

First-Principles Predictions of Thermoelectric Figure of Merit for Organic Materials: Deformation Potential Approximation

Jianming Chen,[†] Dong Wang,^{*,‡} and Zhigang Shuai^{*,†,‡}

[†]Key Laboratory of Organic Solids, Beijing National Laboratory for Molecular Science (BNLMS), Institute of Chemistry, Chinese Academy of Sciences, 100190 Beijing, P. R. China

[‡]MOE Key Laboratory of Organic OptoElectronics and Molecular Engineering, Department of Chemistry, Tsinghua University, 100084 Beijing, P. R. China

ABSTRACT: We propose a combined computational scheme to predict the thermoelectric properties of organic semiconductors, taking α -form phthalocyanine crystals H₂Pc, CuPc, NiPc, and TiOPc as examples. This completely parameter-free approach combines first-principles band structure calculations, Boltzmann transport theory, deformation potential theory for electron–phonon coupling, and nonequilibrium molecular dynamics for heat transport. We abandon the constant relaxation time approximation commonly practiced in the literature. Instead, we calculate it from first principles with the deformation potential approximation. The obtained Seebeck coefficients are in good agreement with experimental results, validating our treatment for relaxation time. From the calculated thermoelectric figure of merit (ZT) value, we show that phthalocyanine crystals could be excellent thermoelectric materials when n-doped, with the highest ZT value of 2.5 in NiPc at a doping level of $-1.5 \times 10^{20} \text{ cm}^{-3}$.

I. INTRODUCTION

Thermoelectric materials interconvert heat energy and electrical energy. Therefore, thermoelectric modules can be built as either power generators or coolers. The energy conversion efficiency of a material is determined by its dimensionless thermoelectric figure of merit $ZT = S^2\sigma T/\kappa$, where σ and κ are the electrical and thermal conductivity and S is the Seebeck coefficient. It indicates that an efficient thermoelectric material must be good at conducting electricity but not heat. That way, a temperature gradient across the material can be maintained instead of the quickly equalizing temperature within the bulk of material. So, in the design of thermoelectric materials, one needs to suppress phonon transport and to enhance electron transport. The concept of a phonon glass electron crystal has been proposed in the search for novel thermoelectric materials.¹ Compounds that have been investigated for thermoelectric applications include skutterudites, half-Heusler alloys, clathrates, and pentatellurides. The best bulk thermoelectric materials available are bismuth telluride alloys as far as their efficiency is concerned. However, the application of such materials is restricted due to the fact that they are toxic and expensive. Recent advances in thermoelectrics demonstrate that an enhanced Seebeck coefficient and reduced thermal conductivity can be achieved in nanostructured materials^{2,3} and nanocomposites.^{4–6} Thermoelectric properties of low-dimensional carbon materials such as carbon nanotubes⁷ and nanowires⁸ have also been studied. Carbon nanotubes conduct electricity and heat equally well, but when wrapped by conducting polymers, the thermal conductivity of nanotubes is reduced to the level of polymers and the Seebeck coefficient remains almost the same.⁹

Compared to inorganic materials, organic electronic materials are usually poor heat conductors, meeting at least one requirement for efficient thermoelectric performance.

Conducting polymers have been studied for thermoelectric applications, such as polyacetylene,^{10,11} polypyrroles,¹² polyanilines,^{13,14} polythiophenes,¹⁵ and poly(2,7-carbazole)s.^{16,17} Enhanced thermoelectric power and electrical conductivity have been observed more in poly(3,4-ethylenedioxythiophene) (PEDOT) nanowires than in thin films.¹⁸ The highest thermoelectric figure of merit reported is 0.25 in PEDOT.¹⁹ In addition to conjugated polymers, thermoelectric properties of thin films of small molecules such as pentacene have been studied by field-effect transistors²⁰ and by the means of doping.²¹

Theoretical and computational efforts have been devoted to the design of and the search for novel thermoelectric materials.^{22–25} Mahan and Sofo²⁶ derived a transport distribution function to give the largest figure of merit and found that a narrow distribution of the energy of the transport electrons is needed for maximum thermoelectric efficiency. Madsen²⁷ proposed an approach that combines first-principles band structure calculations with the Boltzmann transport theory to study the thermoelectric properties of LiZnSb. Zhang and collaborators^{28,29} evaluated the thermoelectric performance of half-Heusler compounds and the filled skutterudites. Nevertheless, very little theoretical work has been performed to predict the thermoelectric performance of organic electronic materials. Earlier, we studied the thermoelectric properties of pentacene and rubrene crystals based on the Boltzmann transport theory, and our results show that a peak figure of merit of 0.5–0.8 can be obtained for the p-doped pentacene crystal.³⁰ The Boltzmann transport theory is applicable when the intermolecular electronic coupling is stronger than the electron–phonon interaction. When the

Received: May 31, 2012

Published: August 6, 2012

electron–phonon interaction is comparable to or even larger than the intermolecular coupling, the Holstein’s small polaron model is appropriate. Recently, Wang et al.³¹ studied the thermoelectric properties of molecular nanowires based on a rigorous evaluation of the Kubo formula using Holstein’s small polaron model. The model relies on a few physical parameters that can be derived either experimentally or theoretically.

In this work, we focus on the thermoelectrics for organic materials predicted from theoretical chemistry. We investigate the thermoelectric properties of phthalocyanine (Pc) and its metal complexes MPc (M = Cu, Ni, and TiO) crystals. Phthalocyanine is a versatile class of organic semiconducting materials with interesting charge transport and optical properties.^{32,33} Early studies reported that the Seebeck coefficient of phthalocyanines falls into the range of 0.6–1.8 mV/K,³⁴ and the Hall measurement demonstrated that the mobility in single crystal phthalocyanines is on the order of cm²/(V s).³⁵ The highest field-effect mobility of holes in thin films of TiOPc is reported to be 10 cm²/(V s), in nice agreement with our theoretical value.³⁶ The high charge carrier mobilities and the large Seebeck coefficients suggest that metal phthalocyanines could be potential thermoelectric materials. Our current research aims at theoretically characterizing thermoelectric properties of phthalocyanine crystals and disclosing a way to optimize the thermoelectric efficiency.

Charge transport in organic materials can be described by either the hopping model or the band model, depending on the magnitude of the electron–phonon coupling with respect to the intermolecular coupling. Often, one employed two parameters, the molecular charge reorganization energy (λ) representing electron-intramolecular vibration coupling versus the intermolecular electronic coupling V (or called hopping integral t). In the case of $V > \lambda$, a band model is more appropriate. Only when $V \ll \lambda$ can the localized charge hopping picture be adopted, which suits a large class of organic molecules.³⁷ From quantum chemistry calculations, it was found that the intermolecular electronic coupling for phthalocyanines can be as large as 0.143 eV, even larger than the intramolecular charge reorganization energy (~ 0.08 eV).³⁶ Thus, in this work, we employ the band description for the electronic structure for phthalocyanines. The transport coefficients are calculated by the Boltzmann transport theory in the relaxation time approximation, with the relaxation time calculated by deformation potential theory.³⁸ The heat transport by phonon is calculated by a nonequilibrium molecular dynamics (NEMD) simulation coupled with a general amber force field (GAFF),³⁹ which we have shown to reproduce the experimental thermal conductivity for pentacene well.⁴⁰

II. METHODOLOGY

Band Structure Calculations. We perform the first-principles calculations with the projector-augmented wave (PAW) method^{41,42} as supplemented in the Vienna ab initio simulation package (VASP).^{43,44} The Perdew–Burke–Ernzerhof (PBE) functional in the generalized gradient approximation (GGA) is applied. The atomic positions in the crystal are further optimized with the quasi-Newton method with the lattice vectors fixed. The energy convergence criterion for the self-consistent cycle is set to be 10^{−4} eV. In the ionic relaxations and charge density calculations, Monkhorst–Pack \mathbf{k} -meshes⁴⁵ of 2 × 12 × 2, 8 × 2 × 2, 3 × 12 × 4, and 6 × 6 × 9 are used for H₂Pc, CuPc, NiPc, and TiOPc, respectively. The smearing

method used for these calculations is the tetrahedron method with Blöchl corrections. For the calculations of transport coefficients, band energies on a much denser \mathbf{k} -mesh are needed. The \mathbf{k} -meshes for H₂Pc, CuPc, NiPc, and TiOPc are 5 × 31 × 5, 35 × 9 × 9, 7 × 25 × 9, and 9 × 9 × 11, respectively, which amount to a total of 388, 1418, 416, and 446 points in the irreducible Brillouin zone. The band energy calculations are not self-consistent; instead, they are based on the charge density obtained from the previous self-consistent calculations on a less dense \mathbf{k} -mesh. The Gaussian smearing method with a width of 0.05 eV is applied in these calculations.

Boltzmann Transport Theory. The Boltzmann transport theory is applied to calculate properties related to the charge carrier transport.⁴⁶ The Boltzmann transport equation describes the time evolution of the charge carrier distribution function in the external fields, such as the electric or magnetic field and the thermal gradient. The charge carriers are subject to the phonon and defect scatterings. These scattering events restore the charge carrier distribution to the original equilibrium state. Relaxation time approximation is usually invoked. The steady-state charge carrier distribution function is then obtained by solving the Boltzmann transport equation. To study doping effects in the thermoelectric materials, we assume that the band structure is not affected by doping and that both n- and p-doping are simulated by a rigid shift of the Fermi level in the distribution function when evaluating the transport coefficients. This rigid band approximation is suitable for low field and low charge carrier concentrations. In the Boltzmann transport theory, the movement of an electron is treated semiclassically, and the group velocity of an electron in a specified band is given by

$$v_{\alpha}(i, \mathbf{k}) = \frac{1}{\hbar} \frac{\partial \varepsilon(i, \mathbf{k})}{\partial k_{\alpha}} \quad (1)$$

where $\varepsilon(i, \mathbf{k})$ is the i th energy band at point \mathbf{k} , k_{α} is the α component of wave vector \mathbf{k} with α the Cartesian index. From the first-principles band structures we obtain the group velocities. Next, we calculate the energy projected transport distribution (TD) tensor

$$\sigma_{\alpha\beta}(\varepsilon) = \frac{e^2}{N} \sum_{i, \mathbf{k}} \tau(i, \mathbf{k}) v_{\alpha}(i, \mathbf{k}) v_{\beta}(i, \mathbf{k}) \delta[\varepsilon - \varepsilon(i, \mathbf{k})] \quad (2)$$

where $\tau(i, \mathbf{k})$ is the relaxation time, α and β are the Cartesian indices, N is the total number of \mathbf{k} points sampled, and e is the elementary charge. The electrical transport tensors are defined as

$$\sigma_{\alpha\beta}(T, \mu) = \frac{1}{\Omega} \int \sigma_{\alpha\beta}(\varepsilon) \left[-\frac{\partial f_0(T, \varepsilon, \mu)}{\partial \varepsilon} \right] d\varepsilon \quad (3)$$

$$S_{\alpha\beta}(T, \mu) = \frac{1}{eT\Omega\sigma_{\alpha\beta}(T, \mu)} \int \sigma_{\alpha\beta}(\varepsilon)(\varepsilon - \mu) \times \left[-\frac{\partial f_0(T, \varepsilon, \mu)}{\partial \varepsilon} \right] d\varepsilon \quad (4)$$

$$\kappa_{\alpha\beta}^0(T, \mu) = \frac{1}{eT\Omega} \int \sigma_{\alpha\beta}(\varepsilon)(\varepsilon - \mu)^2 \times \left[-\frac{\partial f_0(T, \varepsilon, \mu)}{\partial \varepsilon} \right] d\varepsilon \quad (5)$$

where Ω is the volume of the unit cell and f_0 is the equilibrium distribution function, i.e., the Fermi–Dirac distribution function dependent on temperature T and chemical potential μ . It is noticed that the electrical conductivity, the Seebeck coefficient, and the thermal transport coefficient are related to integrals of the zeroth, first, and second order moments of the TD tensor, respectively.⁴⁷ The thermal conductivity contributed by electrons is calculated as

$$\kappa_e = \kappa^0 - S^2 \sigma T \quad (6)$$

The first-principles band energies calculated on a fine \mathbf{k} -mesh are fitted using the method proposed by Madsen;²⁷ then, the velocities on an interpolated \mathbf{k} -mesh are calculated. The TD function and its Fermi integrals as given in eqs 3–5 are then evaluated. The procedures to calculate the electrical transport coefficients are implemented in the BoltzTraP program,⁴⁸ which has been interfaced to the electronic structure package VASP.²⁸ The relaxation times of charge carriers due to phonon scatterings are estimated by the deformation potential theory as presented below.

Deformation Potential Theory. In the application of the Boltzmann transport theory, the relaxation time $\tau(i, \mathbf{k})$ in eq 2 is essential, arising from scattering. It was usually supplied as an empirical parameter, very often estimated from an experimentally measured transport coefficient,⁴⁹ making the computational approach empirical. In our approach, the relaxation time $\tau(i, \mathbf{k})$ is evaluated by the deformation potential theory for treating the electron–phonon scatterings.³⁸ In fact, such an approach has been successfully applied in the calculation of charge carrier mobilities in oligoacene crystals,⁵⁰ graphene,⁵¹ and graphdiyne.⁵² The deformation potential theory describes the electron–acoustic phonon interactions on the assumption that local deformations produced by the lattice waves are close to those in the homogeneously deformed crystals. The scattering probability for electrons from the \mathbf{k} state to the \mathbf{k}' state can be written as

$$|M(\mathbf{k}, \mathbf{k}')|^2 = \frac{E_1^2}{C_{ii}} k_B T \quad (7)$$

where E_1 is the deformation potential constant that represents the energy band shift caused by the crystal lattice deformation, and C_{ii} is the elastic constant in the direction of propagation of the lattice wave. Note that only scatterings contributed by longitudinal acoustic phonons are considered. The relaxation time can be expressed by the scattering probability

$$\frac{1}{\tau(i, \mathbf{k})} = \sum_{\mathbf{k}' \in \text{BZ}} \left\{ \frac{2\pi}{\hbar} |M(\mathbf{k}, \mathbf{k}')|^2 \delta[\varepsilon(i, \mathbf{k}) - \varepsilon(i, \mathbf{k}')] (1 - \cos \theta) \right\} \quad (8)$$

where $\delta[\varepsilon(i, \mathbf{k}) - \varepsilon(i, \mathbf{k}')]$ is the Dirac delta function and θ is the angle between \mathbf{k} and \mathbf{k}' . In Bardeen and Shockley's treatment, it is assumed that scattering is isotropic and the matrix element of interactions $M(\mathbf{k}, \mathbf{k}')$ is independent of \mathbf{k} and \mathbf{k}' . Apparently, this is not true for organic molecular crystals in which the electron–phonon scatterings and the charge carrier transport are anisotropic. To account for the anisotropic scatterings, we simply deform the crystal in three lattice directions and average the scattering probabilities calculated for the three directions.

Phonon Transport. The thermoelectric figure of merit is determined not only by the charge carrier transport, i.e., the electrical transport coefficients, but also by the phonon transport through the lattice thermal conductivity. To evaluate this quantity, we apply the nonequilibrium molecular dynamics method.³⁹ In the NEMD method, a nonequilibrium steady state is prepared by applying a temperature gradient or introducing a heat flux to the system. The lattice thermal conductivity is defined as

$$\kappa_L = -\frac{J}{\nabla T} \quad (9)$$

where J is the heat flux that represents the amount of energy transferred per time and cross-sectional area, κ_L is the lattice thermal conductivity, and ∇T is the temperature gradient. The classical force field is used to describe the inter- and intramolecular interactions that account for the phonon scatterings due to anharmonic lattice vibrations. The simulation box in the direction of heat flow should be large enough to establish the local thermal equilibrium and a sufficient temperature gradient. The periodic boundary conditions have been applied in three directions. The heat flux is generated by the velocity-exchange scheme proposed by Müller-Plathe and Reith.⁵³ That is, the simulation box is divided into N slabs, labeled as slab 0, 1, ..., $N - 1$. The velocities of carbon atoms in slab 0 and $N/2$ are exchanged every few steps in the simulation. To be specific, the hottest carbon atom in slab 0 and the coldest carbon atom in slab $N/2$ are selected, and their velocities are exchanged. This way, a constant heat flow from slab $N/2$ to slab 0 is induced, which results in a temperature gradient. The heat flux imposed in the NEMD simulation can be obtained by

$$J = \frac{1}{2At} \sum_{\text{transfers}} \left(\frac{1}{2} m v_{\text{hot}}^2 - \frac{1}{2} m v_{\text{cold}}^2 \right) \quad (10)$$

where A is the cross-sectional area, m is the mass of a carbon atom, and t is the duration of energy transfer. The simulations are performed with the LAMMPS package.⁵⁴ The GAFF is used to describe the bonded and nonbonded interactions in H_2Pc . The time step used to integrate Newton's equations of motion is set to be 1 fs, and the total NEMD simulation time is 5 ns. The long-range electrostatic interactions are treated by the Ewald/n method as implemented in LAMMPS. To equilibrate the system to the desired temperature, the NEMD simulation is preceded by 0.1 ns of simulation at 300 K where the Berendsen thermostat is applied. The NEMD simulation is carried out for a finite periodic box, and the calculated thermal conductivity has a strong dependence on the box size. This size effect is due to the phonon scatterings at the boundaries of the simulation box. To correct for the size effect, we apply a simple extrapolation scheme. The thermal conductivity obtained from the MD simulation is related to the box size by^{55,56}

$$\frac{1}{\kappa_{\text{MD}}} = \frac{3}{\rho c_v V^2} \tau_{\text{MD}}^{-1} = \frac{3}{\rho c_v V^2} \left(\tau_{\text{bulk}}^{-1} + \frac{2V}{L} \right) \equiv A + \frac{B}{L} \quad (11)$$

where c_v is the specific heat capacity, ρ is the mass density, V is the volume, and τ_{MD} and τ_{bulk} are the phonon relaxation time in the MD simulation and in the true bulk crystal, respectively. The equation shows that the reciprocal of κ_{MD} has a linear relationship with respect to the reciprocal of the box length. We perform NEMD simulations with several box lengths, and then fit the $\kappa_{\text{MD}}^{-1} \sim L^{-1}$ curve to obtain the κ value at the infinite box length.

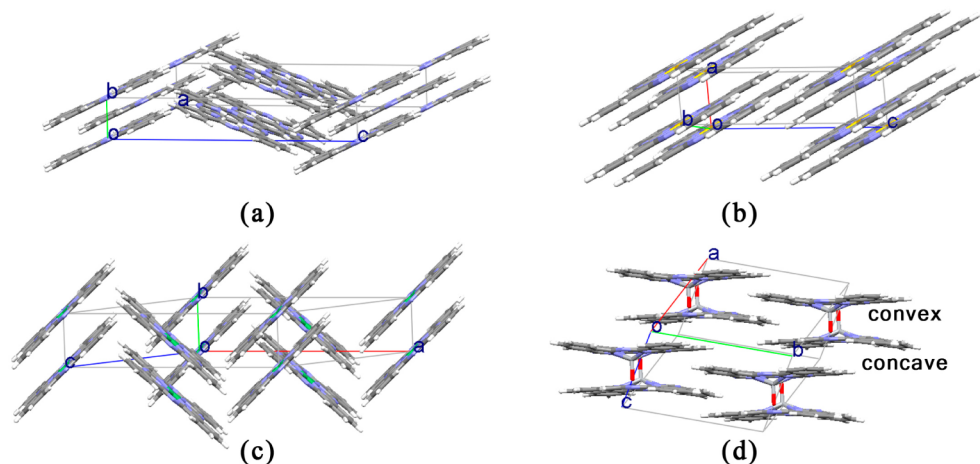


Figure 1. Structures of α -form (a) H_2Pc , (b) CuPc , (c) NiPc , and (d) TiOPc crystals.

III. RESULTS AND DISCUSSION

Band Structures. Phthalocyanine is a macrocyclic compound that can host metal elements in its central cavity. Metal phthalocyanines are known to form various polymorphs in which the molecular stacking arrangements and alignment are profoundly different. The current investigations are focused on α -form H_2Pc , CuPc , NiPc , and TiOPc crystals (Figure 1). The lattice constants of these compounds are listed in Table 1. The

Table 1. Lattice Constants of Phthalocyanine Crystals

	a (Å)	b (Å)	c (Å)	α	β	γ
H_2Pc	26.121	3.797	23.875	90°	94.16°	90°
CuPc	3.805	12.959	12.043	90.64°	95.26°	90.72°
NiPc	19.9	4.71	14.9	90°	121.9°	90°
TiOPc	12.166	12.584	8.641	67.86°	95.03°	96.28°

unit cell of H_2Pc and NiPc is monoclinic with four and two inequivalent molecules in it, and the closest molecular stacking is in the direction of b . The unit cell of CuPc contains one molecule, and the closest molecular packing is in the direction of a . The unit cell of TiOPc is triclinic. It contains two inequivalent molecules that give rise to two types of interactions, namely convex- and concave-type dimers.⁵⁸ H_2Pc , CuPc , and NiPc are planar molecules, but in TiOPc the protruding titanyl groups force the usually planar structure of the phthalocyanine to adopt a nonplanar square pyramidal structure. The convex and concave interactions are determined by the relative orientations of the protruding titanyl groups. The convex interactions involve TiOPc molecules with the titanyl groups facing each other, while the concave interactions with the titanyl groups oriented on opposite sides of the molecules, see Figure 1d. The band structures and the density of states (DOS) of H_2Pc , CuPc , NiPc , and TiOPc are displayed in Figure 2. It is noted that molecular stackings exhibit a profound influence on the band structures. The band gaps of H_2Pc , CuPc , NiPc , and TiOPc are calculated to be 1.179, 1.253, 1.337, and 0.912 eV, respectively. A localized state is observed in the band gap of CuPc . The single electron in this state is immobile, so it does not contribute to the charge carrier transport. This trap state is ignored when the electrical transport properties are calculated. The contribution to the state is analyzed by the projected DOS in Figure 3. It can be seen that the largest contribution is from the d state of the

central copper atom. The calculated DOS diagram of CuPc is compatible with the resonant soft X-ray emission experimental studies reported in ref 56. CuPc is an intrinsic semiconductor even if it contains an odd number of electrons. The experimental band gap of CuPc is about 2.0 eV,³⁵ larger than the calculated one. It has been known that the DFT calculations tend to underestimate the band gaps. Brédas and Norton⁵⁸ investigated the band structures of TiOPc with the PAW method and the GGA PW91 functional. They reported a band gap of 0.92 eV, which is quite close to our result of 0.912 eV using the PBE functional. The experimental band gap is 1.72 eV, obtained with cyclic voltammetry methods performed under inert conditions.⁵⁹ The underestimation of band gaps should have little influence on the charge carrier transport, since it is the bandwidth that determines the transport properties. Though underestimated, there is still an appreciable gap between the conduction and valence bands; therefore when calculating the transport coefficients of electrons, contributions from the valence bands are negligible because they are far from the Fermi level.

The charge carrier transport of holes is governed by the structural feature of the highest valence band, and that of electrons is governed by the lowest conduction band. Large bandwidth is usually a characteristic feature of a high mobility. There are four, two, and two inequivalent molecules in the unit cell of H_2Pc , NiPc , and TiOPc , respectively, so each band in the band structures of H_2Pc appears in a quartet and that of NiPc and TiOPc appears in a pair. The splitting of the sub-bands is small for H_2Pc and NiPc ; that for TiOPc is notably large. The band widths of the valence and conduction bands in high symmetry directions are summarized in Table 2. The valence and conduction bands of H_2Pc exhibit a comparable band dispersion. The width of the conduction band is larger than that of the valence band for CuPc and NiPc , suggesting that the electron mobility is higher than the hole mobility, so CuPc and NiPc are expected to be n-type semiconductors. In contrast, TiOPc exhibits a comparably larger band dispersion at the valence band than the conduction band. The bandwidth of TiOPc in the direction of a along which the crystal has the largest orbital overlap is larger than that in the other two directions. The valence band of NiPc exhibits small band dispersions showing weak electronic couplings between the molecules in the crystal. Sharp DOS is a characteristic feature

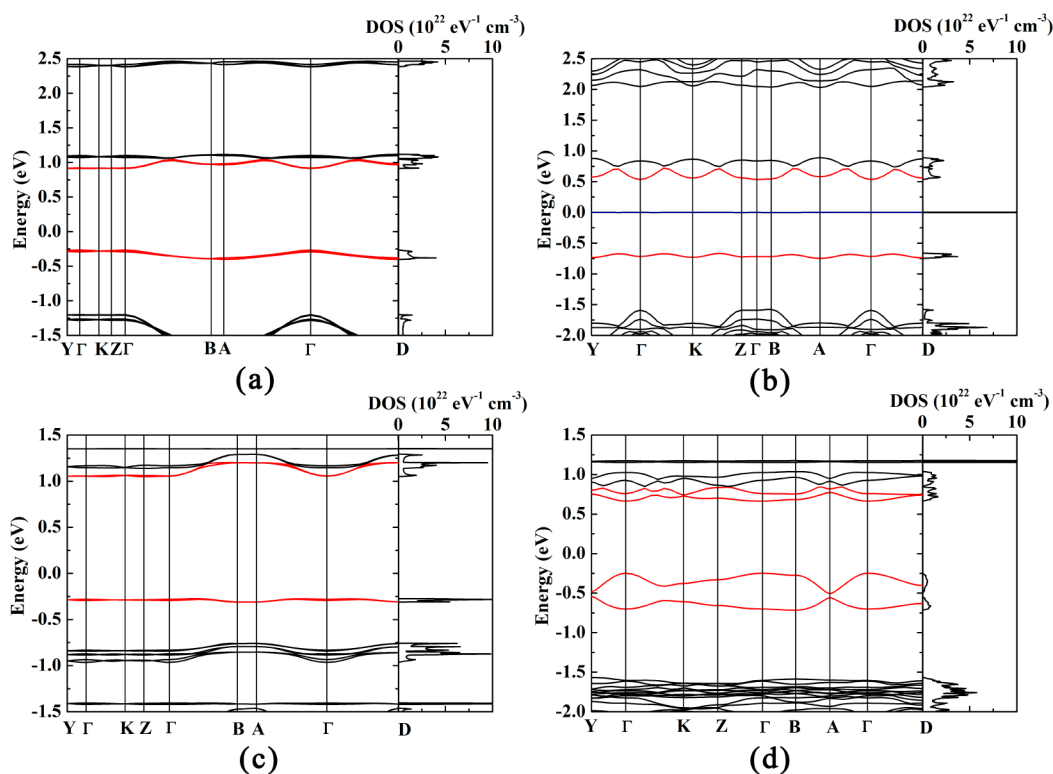


Figure 2. Band structures and DOS for (a) H₂Pc, (b) CuPc, (c) NiPc, and (d) TiOPc. Band energies are shifted so that Fermi levels are at the zero point. The reciprocal coordinates of high-symmetry points are $\Gamma = (0, 0, 0)$, $Y = (0.5, 0, 0)$, $K = (0.5, 0, 0.5)$, $B = (0, 0.5, 0)$, $Z = (0, 0, 0.5)$, $A = (0.5, 0.5, 0)$, and $D = (0.5, 0.5, 0.5)$. The highest valence bands and lowest conduction bands, including all of the sub-bands arising from inequivalent molecules in the unit cell, are highlighted in red.

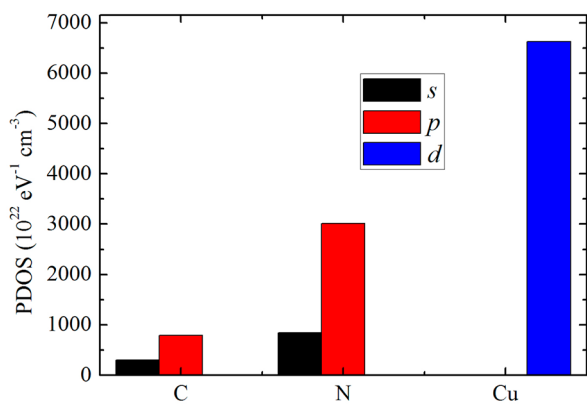


Figure 3. Projected DOS for the localized state of CuPc.

for large Seebeck coefficients, as shown in our previous study on pentacene and rubrene crystals.³⁰

Relaxation Time. The relaxation time measures how quickly an electron restores to the equilibrium distribution via scatterings by phonons, impurities, or other defects. Usually, one employs constant relaxation time approximation, which makes the theory empirical.⁴⁹ We abandon such approximation by calculating the electron–phonon scatterings. We estimate the matrix element of the interactions between electrons and longitudinal acoustic phonons and calculate the relaxation time with the deformation potential theory. To account for the anisotropic scatterings in organic semiconductors, we dilate the lattice in three crystal directions, a , b , and c , and calculate the deformation potential constant E_1 and the elastic constant C_{ii} in three spatial directions. The scattering probabilities $|M(\mathbf{k}, \mathbf{k}')|^2$

of electrons by the acoustic waves in the direction of propagation a , b , and c are averaged and used in the summation over state \mathbf{k}' of eq 8.

To obtain the deformation potential constant E_1 in each direction, we calculate band energies of the lattice deformed in that direction. The displacement of the bottom of the conduction band is used to calculate the deformation potential constant for electrons, and that of the top of the valence band is used for holes. The deformation potential constant is defined as $E_1 = \Delta\varepsilon/(\Delta l/l_0)$, where $\Delta\varepsilon$ is the band edge shift of the conduction and valence bands due to the lattice dilation $\Delta l/l_0$. When not heavily doped, only sub-bands that are near the band edge of the conduction and valence bands contribute to the transport. Since the band edge is usually more sensitive to the lattice deformation than other sub-bands, our calculation only gives an upper limit of the deformation potential constant. We assume that the lowest energy band is not influenced by the lattice deformations, so it is taken as a reference when the band energy shift of the conduction and valence bands is calculated. The deformation potential constants for electrons and holes are given in Table 3. As we can see, the deformation potential constants are indeed anisotropic, due to the anisotropic molecular packings in organic molecular crystals.

The elastic constants are obtained by fitting the total energy of the deformed lattice with respect to the dilation through the relation $\Delta E/V_0 = C_{ii}(\Delta l/l_0)^2/2$, where ΔE is the total energy change due to the dilation $\Delta l/l_0$. The calculated elastic constants of phthalocyanines are provided in Table 4. It is noted that the elastic constants are less anisotropic, and the values of the elastic constants of H₂Pc, CuPc, NiPc, and TiOPc are close to each other. With the deformation potential and the

Table 2. Band Dispersions (meV) in High Symmetry Directions

		$\Gamma\Gamma$	ΓK	KZ	$Z\Gamma$	ΓB	BA	$A\Gamma$	ΓD	whole band
H ₂ Pc	VB4	6	13	6	7	97	10	107	107	120
	VB3	5	2	6	6	108	10	118	118	120
	VB2	7	1	6	6	111	10	101	101	117
	VB1	6	14	6	8	124	10	114	113	124
	CB1	1	2	1	2	115	7	114	114	115
	CB2	1	2	1	1	116	7	119	119	120
	CB3	1	1	1	1	120	7	119	119	121
	CB4	1	2	1	3	124	7	124	123	127
	CuPc	VB1	61	58	64	6	1	64	65	63
CB1		169	182	152	26	8	169	172	163	182
NiPc	VB2	8	7	3	4	28	1	28	25	29
	VB1	6	7	3	4	37	1	35	33	37
	CB1	1	12	13	5	147	2	145	147	152
	CB2	2	7	2	5	146	2	143	145	148
TiOPc	VB2	161	106	48	44	15	161	146	70	176
	VB1	237	165	46	83	25	237	262	155	262
	CB1	90	74	31	36	20	89	109	77	109
	CB2	68	83	94	83	4	86	82	12	100

Table 3. Deformation Potential Constants (eV) for Electrons and Holes of Phthalocyanines

	E_1^a (h)	E_1^b (h)	E_1^c (h)	E_1^a (e)	E_1^b (e)	E_1^c (e)
H ₂ Pc	0.60	1.72	0.93	0.35	0.93	2.03
CuPc	0.31	0.31	0.36	0.26	0.23	1.24
NiPc	0.72	0.03	0.53	0.40	0.69	0.35
TiOPc	1.75	0.59	1.49	0.02	0.36	0.71

Table 4. Elastic Constants of Phthalocyanines (10^9 J m⁻³)

	C_{ii}^a	C_{ii}^b	C_{ii}^c
H ₂ Pc	12.1	8.2	15.9
CuPc	7.8	12.0	11.4
NiPc	11.5	13.2	11.9
TiOPc	13.8	14.0	10.1

elastic constant, we can calculate the relaxation time using eq 8. Since both the deformation potential constant and the elastic constant are anisotropic, the scattering probabilities are anisotropic too. The scattering probability averaged over a , b , and c directions is used to calculate the relaxation time. The relaxation times of phthalocyanine crystals range from several tens of femtoseconds to several hundreds of femtoseconds. It should be noted that the method we used to evaluate the relaxation times is crude. The matrix elements of electron–phonon interactions could be calculated by the density functional perturbation theory,^{60,61} but for organic molecular crystals such calculations are impractical due to the huge demand in computational resources.

Electrical Transport Coefficients. With the band energies and the relaxation time, we can calculate the electrical transport properties of phthalocyanine crystals. Figure 4 shows the Seebeck coefficient S , the electrical conductivity σ , the electronic thermal conductivity κ_e , and the power factor $S^2\sigma$ as a function of the charge carrier concentration at 298 K. The charge carrier concentration is determined by the density of states and the Fermi–Dirac distribution function. The hole concentration is written as

$$N_p = 2 \int_{VB} g(\varepsilon) [1 - f_0(T, \varepsilon, \mu)] d\varepsilon \quad (12)$$

and the electron concentration is

$$N_n = 2 \int_{CB} g(\varepsilon) f_0(T, \varepsilon, \mu) d\varepsilon \quad (13)$$

The charge carrier concentration in Figure 4 is the net concentration that is defined as the difference between the concentration of holes and electrons. As the Fermi level shifts, the dominant charge carriers change between electrons and holes. The net carrier concentration is scaled as negative for n-type doping and positive for p-type doping. The electrical conductivities are apparently anisotropic in phthalocyanine crystals. The conductivity of H₂Pc in the direction of b is much larger than that in the other two directions. This is because the intermolecular distance along the b axis is much shorter than the packing distance along a and c axes, and the π – π stacking in the b direction leads to strong electronic couplings between molecules. Similar situations are found in CuPc and NiPc. The most compact stacking in CuPc is in the direction of a and that of NiPc is in the direction of b . TiOPc exhibits a special anisotropy because its crystal structure is different from the others. The electrical transport in the direction of a and c exhibits a comparably larger conductivity than b owing to the greater molecular overlap in these two directions.

The slope of the linear region of the electrical conductivity versus the charge carrier concentration profiles gives the charge carrier mobility according to $\sigma = \mu eN$. As shown in Figure 4, CuPc and NiPc are distinctly n-type semiconductors because the electron mobility is higher than the hole mobility. These two crystals have a relatively flat valence band and a modestly dispersive conduction band. That makes the electrons transport much easier than the holes. Though the valence band of TiOPc is wider than the conduction band, the holes are more strongly scattered by the acoustic phonons than the electrons because the deformation potential constants for holes are larger than those for electrons (Table 3), so the mobility of holes is less than that of electrons based on our calculations. We notice that the profiles of the electrical conductivity and the electronic contribution to the thermal conductivity exhibit a similar tendency as the charge carrier concentration varies. The Lorentz number $L = \kappa_e/(\sigma T)$ is calculated to be 1.08×10^{-8} , 1.31×10^{-8} , 1.48×10^{-8} , and 2.25×10^{-8} W Ω K⁻² for H₂Pc,

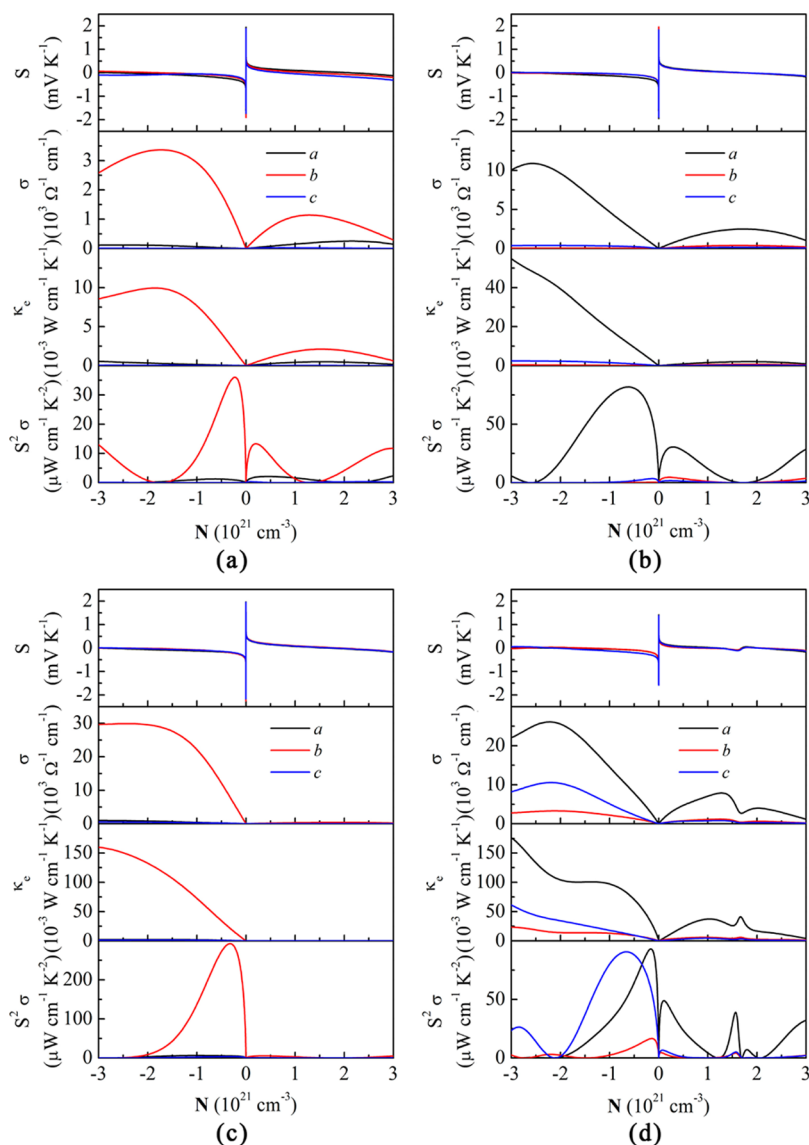


Figure 4. The Seebeck coefficient S , the electrical conductivity σ , the electronic thermal conductivity κ_e , and the thermoelectric power factor $S^2\sigma$ for (a) H_2Pc , (b) CuPc , (c) NiPc , and (d) TiOPc calculated as a function of the charge carrier concentration at 298 K. The charge carrier concentration is positive for p-type doping and negative for n-type doping.

CuPc , NiPc , and TiOPc at a temperature of 298 K and a doping level of $-5 \times 10^{20} \text{ cm}^{-3}$. It is observed that the Lorentz number is not the same for all materials; its value depends on the doping levels, smaller than the theoretical value of $L = (\pi^2/3)(k_B/e)^2 = 2.44 \times 10^{-8} \text{ W } \Omega \text{ K}^{-2}$, which violates the Wiedemann–Franz law. This is because the latter was obtained from free-electron gas model, different from electrons in a band modulated by crystal structure.⁶²

The Seebeck coefficient is positive for holes and negative for electrons. The Seebeck coefficient is isotropic at first glance, and it decreases rapidly as the charge carrier concentration increases. In fact, the Seebeck coefficient decreases linearly with the Fermi level, and the carrier concentration increases exponentially with the Fermi level. In Figure 5, the Seebeck coefficient is plotted as a function of the logarithm of the carrier concentration, and a linear relationship shows up. This is consistent with the thermopower measurement of pentacene and rubrene by the field-effect devices.²⁰ The Seebeck coefficients of phthalocyanine crystals have been measured.³⁴ The α -form H_2Pc , CuPc , and NiPc crystals were reported to

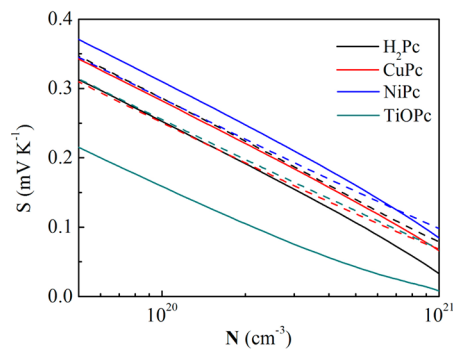


Figure 5. The Seebeck coefficient as a function of the logarithm of the carrier concentration. The solid lines represent holes, and the dashed lines represent electrons. In case of electrons, the absolute value of the Seebeck and the concentration is used.

yield Seebeck coefficient of 1.25, 0.91, and 0.97 mV/K, respectively, at 300 K. The largest Seebeck coefficients of H_2Pc ,

CuPc, NiPc, and TiOPc are calculated to be 1.85, 1.86, 1.49, and 1.38 mV/K for holes and -1.52 , -1.52 , -2.19 , and -1.47 mV/K for electrons, which agrees reasonably well with the experiments. The electron Seebeck coefficient of NiPc is the largest in magnitude and the hole Seebeck of TiOPc is the smallest. Overall, the differences in the Seebeck coefficients are not appreciably large among the phthalocyanine crystals, nor is it between electrons and holes.

As the carrier concentration increases, the electrical conductivity increases and the thermopower decreases; the thermoelectric power factor shows a peak value at certain carrier concentrations. So doping is one of the effective ways to control the thermoelectric performance of a material. Controlled p-doping of phthalocyanines by strong electron acceptors has been investigated by combined Seebeck and conductivity measurements.^{63,64} A novel n-type doping technique by strong donors has been developed to enable the n-type conduction in metallophthalocyanines.⁶⁵ The power factors of n-doped phthalocyanines are higher than those of p-doped, suggesting that all phthalocyanine crystals studied are n-type thermoelectric materials. The maximum power factors of H₂Pc, CuPc, NiPc, and TiOPc reach a magnitude of 36.0, 81.7, 292.8, and 93.1 $\mu\text{W cm}^{-1} \text{K}^{-2}$, respectively.

Lattice Thermal Conductivity. The thermal conductivity has two contributions, one due to electrons and the other due to phonons. The lattice thermal conductivity is caused by the anharmonicity in lattice vibrations that can be characterized by the classical force fields. To estimate the dimensionless figure of merit, the lattice thermal conductivity is calculated. We only evaluate the lattice thermal conductivity of H₂Pc in the direction of *b*, along which the largest power factor is observed. We build super cells with reasonable lengths in the direction of *b*. Each super cell is divided into 20 layers, labeled as layers 0, 1, ..., 19 from left to right, and 5 ns of NEMD simulations are performed. The local temperature of layers 0 to 10 and the instantaneous temperature for layer 0, the heat sink, and layer 10, the heat source, are plotted in Figure 6. One can find that as

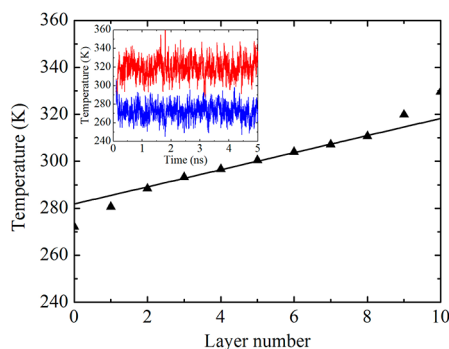


Figure 6. Temperature profile obtained from NEMD simulations for box dimensions of $1 \times 25 \times 1$. The solid line is a linear fit of the data. Inset: instantaneous temperature of the heat sink (blue) and source (red) as a function of simulation time.

the simulation proceeds, the temperature of layer 0 goes down, and that of layer 10 goes up. After 1 ns, a steady state and the local thermal equilibrium have been reached. The local temperature of each layer is obtained by taking an average over trajectories from 1 to 5 ns. Since periodical boundary conditions have been applied, heat actually flows in two opposite directions. So layers 1 and 19, layers 2 and 18, and so on are equivalent in the sense of temperature. The local

temperature of layer 1 in Figure 6 is taken as the average temperature of layers 1 and 19. A good linear relationship between temperature and the layer number is shown except for the region of the heat sink and source, which indicates that in that region the unphysical exchange of atomic velocities and the physical heat flow in the system are not well balanced. The linear region of the temperature profile is fitted to obtain the temperature gradient. The heat current is calculated by the energy exchanged via eq 10. With heat current and temperature gradient, we can derive the lattice thermal conductivity using Fourier's law given in eq 9.

To correct the boundary scattering effect, we carry out NEMD simulations with box lengths of 25, 30, 35, 40, 50, and 55 unit cells in the direction of *b*. The inverse of the lattice thermal conductivity κ_L^{-1} versus the inverse of the box length L^{-1} is plotted in Figure 7. Equation 11 is used to fit the

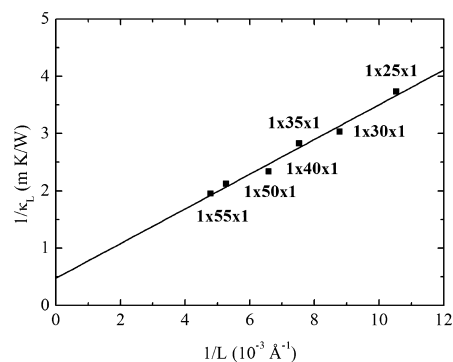


Figure 7. Inverse of the thermal conductivity as a function of the inverse of the box length for H₂Pc. The heat flow is in the direction of *b**. Linear regression of the data yields the bulk thermal conductivity of H₂Pc in the direction of *b**, which is 2.1 W/mK.

simulation results. From the intercept of the fitted line, we can extract the bulk lattice thermal conductivity of H₂Pc in the direction of *b**, which is 2.1 W/mK. The phonon transport in organic molecular crystals is anisotropic, and the largest lattice thermal conductivity is usually in the direction in which the molecular packing is the closest, as we have seen in the pentacene crystal in our earlier investigation.⁴⁰ Since the closest packing arrangement in H₂Pc is in the direction of *b*, we expect that the lattice thermal conductivity is the largest in that direction. The lattice thermal conductivities of other metal phthalocyanines are approximated with that of H₂Pc in the evaluation of ZT.

Dimensionless Figure of Merit. Combining the lattice thermal conductivity and the electrical transport coefficients, we can estimate the ZT of H₂Pc, CuPc, NiPc, and TiOPc. The ZT value at 298 K as a function of carrier concentration is shown in Figure 8. The crystal direction along which the power factor is the largest is of interest, and it is the *b*, *a*, *b*, and *a* directions for H₂Pc, CuPc, NiPc, and TiOPc, respectively. Since the lattice constant of three metalphthalocyanines in the directions of *a*, *b*, and *a* is comparable to or larger than that of H₂Pc in the direction of *b*, we assume that the lattice thermal conductivity of H₂Pc gives an upper limit of the lattice thermal conductivity of other phthalocyanines. The lattice thermal conductivity used to calculate ZT is that of H₂Pc in the direction of *b**, which is 2.1 W/mK. As we can see, all phthalocyanine bulk crystals can reach a maximum ZT whether n-doped or p-doped, but apparently the dimensionless figure of merit of phthalocyanines

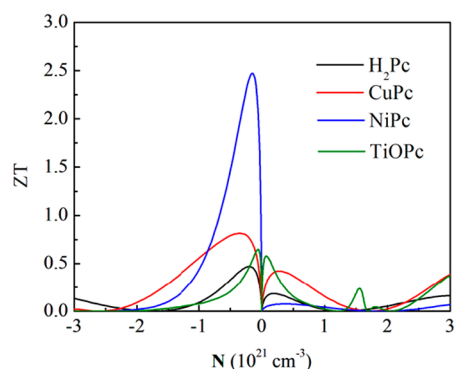


Figure 8. Dimensionless figure of merit versus the carrier concentration for H₂Pc, CuPc, NiPc, and TiOPc. The lattice thermal conductivity used for the estimation of ZT is 2.1 W/mK.

is higher for n-doping. Along the *b* axis, the ZT value of H₂Pc can reach 0.5 with a doping level of $-2.0 \times 10^{20} \text{ cm}^{-3}$, in the case of CuPc, along the *a* axis the ZT can reach 0.8 with a doping level of $-3.5 \times 10^{20} \text{ cm}^{-3}$. The ZT value of NiPc shows a peak value of 2.5 at a carrier concentration of $-1.5 \times 10^{20} \text{ cm}^{-3}$, and that of TiOPc has a maximum value of 0.6 at a carrier concentration of $-1.0 \times 10^{20} \text{ cm}^{-3}$. Among these phthalocyanines, NiPc exhibits the highest figure of merit, and it is an n-type thermoelectric material.

The crystals of H₂Pc, CuPc, and NiPc do not show essential ZT when p-doped. This can be attributed to the fact that the Seebeck coefficients for electrons and holes are close in magnitude, but the charge carrier mobility of holes is much lower than that of electrons, especially in the case of NiPc. The Seebeck coefficients are slightly different among these phthalocyanines, but the electron mobility in NiPc is much higher than that in H₂Pc and CuPc. So the best thermoelectric performance is observed in NiPc. TiOPc has a charge carrier mobility comparable to NiPc, but the Seebeck coefficient of TiOPc is lower than that of NiPc, so the power factor and ZT of TiOPc are lower than those of NiPc. For TiOPc, the electron mobility is just slightly higher than the hole mobility, so the ZT value when p-doped is only slightly lower than that when n-doped. TiOPc is the only p-type thermoelectric material with a ZT of 0.6. From the discussions above, we show that the thermoelectric performance of semiconducting phthalocyanine crystals can be improved by dopings, and the accurate control of the doping level can turn NiPc into an effective n-type thermoelectric material.

IV. CONCLUSIONS

To summarize, we have proposed a parameter-free computational scheme that combines the first-principles band structure calculations, the Boltzmann transport theory, the deformation potential theory, and the nonequilibrium molecular dynamics simulations to predict the thermoelectric property for organic molecular crystals. The relaxation time is now calculated at the first-principles level, instead of assuming a constant estimated from experiments as commonly practiced. This method is applied to investigate the thermoelectric properties of phthalocyanine crystals including H₂Pc, CuPc, NiPc, and TiOPc. The Seebeck coefficients are found to be in good agreement with the experiments, validating our assumption of energy band description for such closely packed organic materials as well as the electron–phonon relaxation time described by deformation potential approximation. It is found

that phthalocyanines could be efficient n-type thermoelectric materials when doped with electron donors. The central metal atom and the molecular packing in phthalocyanine crystals show profound influences on the thermoelectric transport properties. The thermoelectric figure of merit at the optimal doping level ranges from 0.5 for H₂Pc to 2.5 for NiPc when n-doped. The optimal thermoelectric material is found to be NiPc, which exhibits both high electron mobility and large Seebeck coefficient. Our study suggests that organic molecular crystals can show promising thermoelectric figures of merit through controlling the doping level. Our results and the doping level predicted are useful in the search for efficient organic thermoelectric materials. It should be pointed out that the present approach does not take the charge localization effect into account, or polaron effect.³¹ When considering doping, since the bandwidth for organic semiconductors is usually narrow, the carrier scattering effect could also be important, in addition to scattering/relaxation with static and dynamic disorders and impurities. All of these impose interesting challenges for further investigation.

■ AUTHOR INFORMATION

Corresponding Author

*E-mail: dong913@tsinghua.edu.cn, zgshuai@tsinghua.edu.cn.

Notes

The authors declare no competing financial interest.

■ ACKNOWLEDGMENTS

This work is supported by the National Science Foundation of China (Grant Nos. 20920102031 and 20903060) and the Ministry of Science and Technology of China (Grant Nos. 2009CB623600, 2011CB932304, and 2011CB808405). The Supercomputing Center of the Chinese Academy of Sciences is gratefully acknowledged for providing computational resources for large-scale MD simulations.

■ REFERENCES

- (1) Snyder, G. J.; Christensen, M.; Nishibori, E.; Caillat, T.; Iversen, B. B. *Nat. Mater.* **2004**, *3*, 458–463.
- (2) Bux, S. K.; Fleurial, J.-P.; Kaner, R. B. *Chem. Commun.* **2010**, *46*, 8311–8324.
- (3) Tang, J. Y.; Wang, H.-T.; Lee, D. H.; Fardy, M.; Huo, Z. Y.; Russell, T. P.; Yang, P. D. *Nano Lett.* **2010**, *10*, 4279–4283.
- (4) Jood, P.; Mehta, R. J.; Zhang, Y.; Peleckis, G.; Wang, X.; Siegel, R. W.; Borca-Tasciuc, T.; Dou, S. X.; Ramanath, G. *Nano Lett.* **2011**, *11*, 4337–4342.
- (5) Marconnet, A. M.; Yamamoto, N.; Panzer, M. A.; Wardle, B. L.; Goodson, K. E. *ACS Nano* **2011**, *5*, 4818–4825.
- (6) Yu, C.; Kim, Y. S.; Kim, D.; Grunlan, J. C. *Nano Lett.* **2008**, *8*, 4428–4432.
- (7) Robert, C.; Cola, B. A.; Fisher, T.; Xu, X. F.; Gall, K.; Graham, S. *Nanotechnology* **2010**, *21*, 445705.
- (8) Liang, W. J.; Rabin, O.; Hochbaum, A.; Fardy, M.; Zhang, M. J.; Yang, P. D. *Nano Res.* **2009**, *2*, 394–399.
- (9) Meng, C.; Liu, C.; Fan, S. *Adv. Mater.* **2010**, *22*, 535–539.
- (10) Pukacki, W.; Plochanski, J.; Roth, S. *Synth. Met.* **1994**, *62*, 253–256.
- (11) Zuzok, R.; Kaiser, A. B.; Pukacki, W.; Roth, S. *J. Chem. Phys.* **1991**, *95*, 1270–1275.
- (12) Maddison, D. S.; Unsworth, J.; Roberts, R. B. *Synth. Met.* **1988**, *26*, 99–108.
- (13) Li, J.; Tang, X.; Li, H.; Yan, Y.; Zhang, Q. *Synth. Met.* **2010**, *160*, 1153–1158.
- (14) Sun, Y. M.; Wei, Z. M.; Xu, W.; Zhu, D. B. *Synth. Met.* **2010**, *160*, 2371–2376.

- (15) Lu, B.-Y.; Liu, C.-C.; Lu, S.; Xu, J.-K.; Jiang, F.-X.; Li, Y.-Z.; Zhang, Z. *Chin. Phys. Lett.* **2010**, *27*, 057201.
- (16) Aich, R. B.; Blouin, N.; Bouchard, A.; Leclerc, M. *Chem. Mater.* **2009**, *21*, 751–757.
- (17) Dubey, N.; Leclerc, M. *J. Polym. Sci., Part B: Polym. Phys.* **2011**, *49*, 467–475.
- (18) Scholdt, M.; Do, H.; Lang, J.; Gall, A.; Colsmann, A.; Lemmer, U.; Koenig, J.; Winkler, M.; Boettner, H. *J. Electron. Mater.* **2010**, *39*, 1589–1592.
- (19) Bubnova, O.; Khan, Z. U.; Malti, A.; Braun, S.; Fahlman, M.; Berggren, M.; Crispin, X. *Nat. Mater.* **2011**, *10*, 429–433.
- (20) Pernstich, K. P.; Rössner, B.; Batlogg, B. *Nat. Mater.* **2008**, *7*, 321–325.
- (21) Harada, K.; Sumino, M.; Adachi, C.; Tanaka, S.; Miyazaki, K. *Appl. Phys. Lett.* **2010**, *96*, 253304.
- (22) Baxendale, M.; Lim, K. G.; Amaratunga, G. A. *J. Phys. Rev. B* **2000**, *61*, 12705.
- (23) Heremans, J. Nanometer-Scale Thermoelectric Materials. In *Springer Handbook of Nanotechnology*; Bhushan, B., Ed; Springer: Berlin, 2007; pp 345–374.
- (24) Snyder, G. J.; Toberer, E. S. *Nat. Mater.* **2008**, *7*, 105–114.
- (25) Zheng, J.-C. *Front. Phys. China* **2008**, *3*, 269–279.
- (26) Mahan, G. D.; Sofo, J. O. *Proc. Natl. Acad. Sci. U.S.A.* **1996**, *93*, 7436–7439.
- (27) Madsen, G. K. H. *J. Am. Chem. Soc.* **2006**, *128*, 12140–12146.
- (28) Yang, J.; Li, H. M.; Wu, T.; Zhang, W. Q.; Chen, L. D.; Yang, J. H. *Adv. Funct. Mater.* **2008**, *18*, 2880–2888.
- (29) Shi, X.; Yang, J.; Salvador, J. R.; Chi, M. F.; Cho, J. Y.; Wang, H.; Bai, S. Q.; Yang, J. H.; Zhang, W. Q.; Chen, L. D. *J. Am. Chem. Soc.* **2011**, *133*, 7837–7846.
- (30) Wang, D.; Tang, L.; Long, M. Q.; Shuai, Z. G. *J. Chem. Phys.* **2009**, *131*, 224704.
- (31) Wang, Y. Y.; Zhou, J.; Yang, R. G. *J. Phys. Chem. C* **2011**, *115*, 24418–24428.
- (32) Chen, W.; Chen, S.; Chen, S.; Huang, Y. L.; Huang, H.; Qi, D. C.; Gao, X. Y.; Ma, J.; Wee, A. T. S. *J. Appl. Phys.* **2009**, *106*, 064910.
- (33) Chakrabarti, S.; Dey, S.; Pal, A. *J. Appl. Phys. Lett.* **2011**, *99*, 053308.
- (34) Hamann, C.; Storbeck, I. *Naturwissenschaften* **1963**, *50*, 327–327.
- (35) Heilmeyer, G. H.; Harrison, S. E. *Phys. Rev.* **1963**, *132*, 2010–2016.
- (36) Li, L. Q.; Tang, Q. X.; Li, H. X.; Yang, X. D.; Hu, W. P.; Song, Y. B.; Shuai, Z. G.; Xu, W.; Liu, Y. Q.; Zhu, D. B. *Adv. Mater.* **2007**, *19*, 2613–2617.
- (37) (a) Shuai, Z. G.; Wang, L. J.; Li, Q. K. *Adv. Mater.* **2011**, *20*, 1145–1153. (b) Geng, H.; Peng, Q.; Wang, L. J.; Li, H. J.; Liao, Y.; Ma, Z. Y.; Shuai, Z. G. *Adv. Mater.* **2012**, *24*, 3568–3572.
- (38) Bardeen, J.; Shockley, W. *Phys. Rev.* **1950**, *80*, 72–80.
- (39) Wang, J.; Wolf, R. M.; Caldwell, J. W.; Kollman, P. A.; Case, D. A. *J. Comput. Chem.* **2004**, *25*, 1157–1174.
- (40) Wang, D.; Tang, L.; Long, M. Q.; Shuai, Z. G. *J. Phys. Chem. C* **2011**, *115*, 5940–5946.
- (41) Blöchl, P. E. *Phys. Rev. B* **1994**, *50*, 17953–17979.
- (42) Kresse, G.; Joubert, D. *Phys. Rev. B* **1999**, *59*, 1758–1775.
- (43) Kresse, G.; Furthmüller, J. *Comput. Mater. Sci.* **1996**, *6*, 15–50.
- (44) Kresse, G.; Furthmüller, J. *Phys. Rev. B* **1996**, *54*, 11169–11186.
- (45) Monkhorst, H. J.; Pack, J. D. *Phys. Rev. B* **1976**, *13*, 5188–5192.
- (46) Ziman, J. M. *Principles of the Theory of Solids*; Cambridge University Press: Cambridge, U.K., 1964.
- (47) Fan, Z.; Wang, H.-Q.; Zheng, J.-C. *J. Appl. Phys.* **2011**, *109*, 073713.
- (48) Madsen, G. K. H.; Singh, D. J. *Comput. Phys. Commun.* **2006**, *175*, 67–71.
- (49) Allen, P. B.; Pickett, W. E.; Krakauer, H. *Phys. Rev. B* **1988**, *37*, 7482–7490.
- (50) Tang, L.; Long, M. Q.; Wang, D.; Shuai, Z. G. *Sci. China, Ser. B* **2009**, *52*, 1646–1652.
- (51) Long, M. Q.; Tang, L.; Wang, D.; Wang, L. J.; Shuai, Z. G. *J. Am. Chem. Soc.* **2009**, *131*, 17728–17729.
- (52) Long, M. Q.; Tang, L.; Wang, D.; Li, Y. L.; Shuai, Z. G. *ACS Nano* **2011**, *5*, 2593–2600.
- (53) Müller-Plathe, F.; Reith, D. *Comput. Theor. Polym. Sci.* **1999**, *9*, 203–209.
- (54) Plimpton, S. J. *Comput. Phys.* **1995**, *117*, 1–19. <http://lammps.sandia.gov> (accessed July 9, 2009)
- (55) Schelling, P. K.; Phillpot, S. R.; Keblinski, P. *Phys. Rev. B* **2002**, *65*, 144306.
- (56) Jiang, H.; Myshakin, E. M.; Jordan, K. D.; Warzinski, R. P. *J. Phys. Chem. B* **2008**, *112*, 10207–10216.
- (57) Downes, J. E.; McGuinness, C.; Glans, P.-A.; Learmonth, T.; Fu, D.; Sheridan, P.; Smith, K. E. *Chem. Phys. Lett.* **2004**, *390*, 203–207.
- (58) Norton, J. E.; Brédas, J.-L. *J. Chem. Phys.* **2008**, *128*, 034701.
- (59) Kong, X.-H.; Wang, M.; Lei, S.-B.; Yang, Y.-L.; Wang, C. J. *Mater. Chem.* **2006**, *16*, 4265–4269.
- (60) Baroni, S.; Giannozzi, P.; Testa, A. *Phys. Rev. Lett.* **1987**, *58*, 1861–1864.
- (61) Baroni, S.; de Gironcoli, S.; Dal Corso, A.; Giannozzi, P. *Rev. Mod. Phys.* **2001**, *73*, 515–562.
- (62) Minnich, A. J.; Dresselhaus, M. S.; Ren, Z. F.; Chen, G. *Energy Environ. Sci.* **2009**, *2*, 466–479.
- (63) Pfeiffer, M.; Beyer, A.; Fritz, T.; Leo, K. *Appl. Phys. Lett.* **1998**, *73*, 3202–3204.
- (64) Pfeiffer, M.; Fritz, T.; Blochwitz, J.; Nollau, A.; Plönnigs, B.; Beyer, A.; Leo, K. Controlled doping of molecular organic layers: Physics and device prospects. In *Advances in Solid State Physics*, Kramer, B., Ed; Springer: Berlin, 1999; Vol. 39, pp 77–90.
- (65) Harada, K.; Werner, A. G.; Pfeiffer, M.; Bloom, C. J.; Elliott, C. M.; Leo, K. *Proc. SPIE* **2004**, *5464*, 1–9.